DOI: 10.17344/acsi.2019.4937 *Acta Chim. Slov.* **2019,** *66,* 584–591

Scientific paper

Synthesis of Copper-Doped MnO_2 Electrode Materials by One-Step Hydrothermal Method for High Performance

Dongxia An,[1] Yu Zhang,[1] Hong Zhang,[1] Gang Ma,[1] Cuimiao Zhang[1] and Zhiguang Ma[1,2,*]

[1] *College of Chemistry and Environmental Science, Hebei University, Baoding 071002, China*

[2] *Key Laboratory of Chemical Biology of Hebei Province, Hebei University, Baoding 071002, China*

Tel.: +86-312-5079359 Fax: +86-312-5079525

Received: 01-06-2019

Abstract

By adjusting the amount of $Cu(NO_3)_2{\cdot}3H_2O$, Cu^{2+}-doped birnessite δ-MnO_2 spherical substances were synthesized by a simple hydrothermal synthesis process without any templates and surfactants. The structure, morphology, and specific surface area were characterized by XRD, SEM, TEM and BET. Further study shows that the 0.25 mmol Cu-doped MnO_2 sample is expected to provide higher specific capacitance (636.3 F g^{-1} at 1 A g^{-1} current density) compared with pure δ-MnO_2 (335.6 F g^{-1} at the current density of 1 A g^{-1}) and long-term cyclic stability (105.01% capacitance retention after 1500 cycles at current density of 5 A g^{-1}). Electrochemical impedance spectroscopy proved the low resistance characteristics of the prepared samples. All the results show that the copper-doped MnO_2 material is not only low cost, but also of excellent electrochemical performance, thus possesses great potential in future energy development.

Keywords: Copper-doped MnO_2; hydrothermal method; supercapacitor

1. Introduction

The increasing environmental problems and the consumption of natural energy resources such as coal, natural gas and oil have created the need to develop green and sustainable energy sources that have the capacity to convert and store energy. Researchers have been focused on the development of energy storage devices, such as capacitors, batteries, supercapacitors and batteries.[1–5] Among various energy storage devices, supercapacitors(Scs) is a new type of environmentally friendly energy storage device with high power density (more than 10 kw kg^{-1}), fast charge and discharge speed, long cycle life (>10^5 cycles),[6–9] etc. Yet, in order to meet the requirements of rapid growing technology, supercapacitor also faces some challenges, such as low energy density and short lifespan.[10–13] There are two types of energy storage mechanisms for supercapacitors, double-layer capacitors and pseudo-capacitors. The common electrode material used for double-layer capacitors is carbon material. Whereas, transition metal oxides are the most commonly used materials for pseudo-capacitors.[7,14,15] Many researchers have been working on transition metal oxides, which exhibit high specific capacitance and good stability for pseudocapacitors.[16–19] So far, various transition metal oxides have been used as electrode materials in pseudocapacitors, including Co_3O_4,[20] MnO_2,[21] NiO,[22,23] RuO_2,[24] V_2O_5,[25] etc. Compared with other transition metal oxides, MnO_2 has the advantages of low cost, high natural abundance, high theoretical capacity (1370 Fg^{-1}), high voltage window, etc.[26–31] It is considered to be the most promising electrode material. However, its capacitance is much lower and its conductivity and structural stability are also relatively poor which restricts its application in real world.[32] In order to improve these problems, MnO_2 has been combined with other materials to obtain good electrochemical performance, such as graphene@MnO_2,[33] carbon nanotubes@MnO_2,[34,35] CuO@MnO_2,[36] Co_3O_4@MnO_2[37,38] nanocomposites. Moreover, cationic doping has been proved to be an effective way to improve the conductivity of materials. As an effective doped cation, copper cations are considered as one of the most suitable candidates for cationic doping to improve electrochemical performance.[39] However, it is still a challenge to obtain high-performance MnO_2 electrode materials with a simple and low cost preparation

process. In addition, Cu-doped MnO_2 is also used in other applications, such as the nanostructured copper manganese oxide (CMO) thin films[40] and selective absorbers.[41]

In this work, we designed and prepared Cu^{2+}-doped MnO_2 by a simple one-step hydrothermal method. X-ray powder diffraction (XRD), scanning electron microscopy (SEM) and transmission electron microscopy (TEM) were used to analyze the morphology and microstructure of the samples. The electrochemical test results showed that the capacitance of 0.25 mmol Cu^{2+}-doped MnO_2 mixed electrode was 636.3 F g^{-1} at 1 A g^{-1} current density and the capacitance retention was 105.01% after 1500 cycles at current density of 5 A g^{-1}.

2. Experimental

2. 1. Synthesis of Cu^{2+} Doped MnO_2

All chemicals used in this experiment were analytical grade. MnO_2 was synthesized using a typical hydrothermal method. Firstly, $KMnO_4$ and $MnSO_4$ (the molar ratio of 3:1) were added into deionized water (25 mL) respectively and stirred continuously. Then, $Cu(NO_3)_2 \cdot 3H_2O$ salt of various doping contents (0.1, 0.25, 0.35, 0.45 mmol) was added into the above potassium permanganate solution during the stirring stage. Then, the manganese sulfate solution was slowly poured into the mixture. The mixture was stirred continuously until the solid was completely dissolved at room temperature, and a piece of the pretreated foam nickels were put vertically into the autoclave. The resultant product was transferred into a Teflon-lined stainless-steel auto-clave and heated to 80 ° for 3 h. Lastly, the vessel was allowed to be cooled to room temperature naturally and the NFs substrate with the active materials were taken out and labeled as M1, the brown precipitates were collected and washed with distilled water and ethanol for several times, then the filtrate were dried at 60° for 12 h under vacuum.

2. 2. Characterization

The surface morphology and microstructure of samples were characterized by field emission scanning electron microscope (SEM, JSM-7500F) and transmission electron microscopy (TEM, Tecnai G2 F20 S-TWIN). The X-ray powder diffraction (XRD) measurements were performed on Bruker D8 Advance. N_2 absorption-desorption were performed with a Micromeritics TristarII 3020. The surface area was computed from the Brunauer–Emmett-Teller (BET) equation, and the pore size distribution was calculated from desorption curve by the Barrette-Joynere-Halenda (BJH) model.

2. 3. Electrochemical Measurement

Electrochemical properties were measured in a three electrode system employing the Electrochemical Workstation (INTERFACE 1000, GAMRY, US) in which the NF-Cu-MnO_2 was used as working electrode, saturated calomel electrode (SCE) as a reference electrode and a platinum wire as counter electrode. Cyclic voltammetry (CV), galvanostatic charge–discharge (GCD) and electrochemical impedance spectra (EIS) were performed using workstation in 1 mol L^{-1} KOH electrolyte. The capacitance formula is:

$$C_m = \frac{I\Delta t}{m\Delta V} \quad (1)$$

where I/m is the current density, t is the discharge time, V is the potential window, and m is the mass of the MnO_2 material.

3. Results and Discussion

3. 1. Structure and Morphology

The X-ray diffraction (XRD) patterns of the two samples are shown in Figure. 1 to determine the phase composition of the product , in which curve A represents the pure MnO_2 sample and B represents the 0.25 mmol Cu^{2+}-doped MnO_2 sample. It can be clearly seen from curve A that the main characteristic peaks are located at 12.9°, 37.3° and 65.6° which correspond to the (001) ($^{-1}$11) and (020) planes of MnO_2, respectively. These characteristic peaks indicate that the sample belongs to the birnessite δ-MnO_2 structure. The wide and weak reflection peaks can be seen from the XRD patterns, indicating that the structure of pure MnO_2 is amorphous. The XRD pattern is in good agreement with the diffraction peaks reported in JCPDS card no. 80–1098.[42] In addition, it can be clearly seen from curve B that it also shows peaks at 26.1° and 55.9° of the plane corresponding to the (011), (0–24) planes of $CuSO_4 \cdot H_2O$ (JCPDS 21–0269). At the same

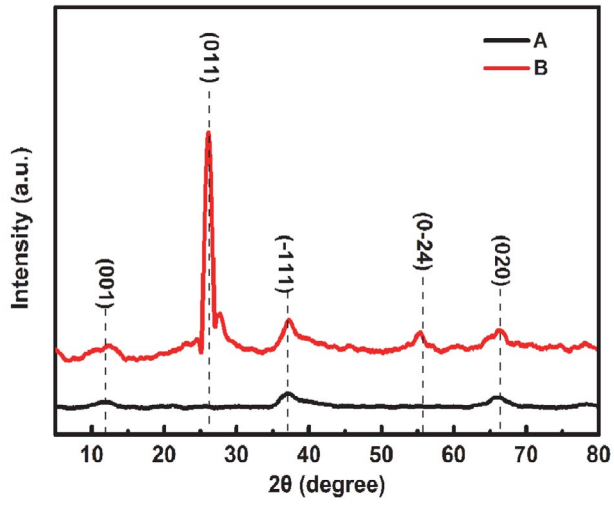

Fig1. XRD patterns of the samples.

time, it can be seen that the peak at 011 corresponds to the crystal structure of $CuSO_4 \cdot H_2O$ formed in amorphous manganese dioxide. δ-MnO_2 has a two-dimensional(2D) layered structure, which is considered to be a convenient structure to promote the migration of metal ions or water molecules and to allow ions and water molecules to exist in the inter-laminar region.[43] Due to the relatively open layered structure, Cu^{2+} and SO_4^{2-} are embedded in the structure of MnO_2.

The morphologies of pure MnO_2 and 0.25 mmol Cu^{2+} doped-MnO_2 electrodes were investigated by scanning electron microscopy (SEM) and transmission electron microscopy (TEM). Figure. 2 shows the SEM and TEM images of MnO_2 and 0.25 mmol Cu^{2+}-doped MnO_2 electrodes. As can be seen from Figure 2a and 2b, the synthesized pure MnO_2 and 0.25 mmol Cu^{2+}-doped MnO_2 showed a surface morphology similar to that of a micro-flower consisting of a stack of vertically aligned thin nanosheets. It can be seen that there is no difference between the morphology of the two samples, which may be due to the fact that the amount of Cu^{2+} doped is too small to affect the morphology of MnO_2. Figures 2c and 2d show TEM images of MnO_2 and 0.25 mmol Cu^{2+} doped MnO_2. As can be seen from the figure, the internal structure of the gate of the synthetic material is that the ultrathin nanosheets are connected to each other to form a layered and porous 3D structure. However, compared to MnO_2 (Fig. c), the internal structure of MnO_2 doped with Cu^{2+} (Fig. d) is made by more compact ultrathin nanosheets.

Figure. 3 shows the N_2 adsorption-desorption isotherms of MnO_2 and 0.25 mmol Cu^{2+} doped MnO_2. It can be seen from the diagram that the isotherm can be identified as type III, which can be attributed to the slit pores formed by the self-assembled nanocrystals. There is no obvious narrow hysteresis ring between the two substances at relatively low pressure which also indicates that the porous characteristics of the sample are open and the capillary condensation of nitrogen has no significant delay. However, 0.25 mmol Cu^{2+} doped MnO_2 has obvious hysteresis loops in the region of relative high pressure (P / P_0

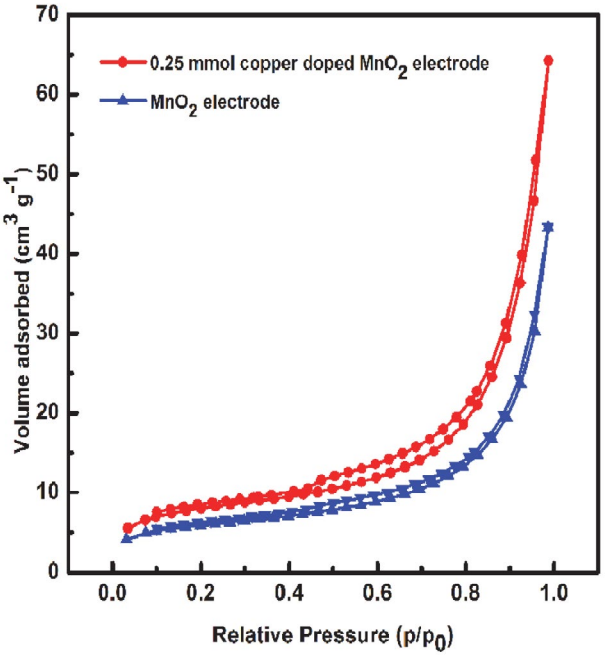

Fig. 3. Nitrogen adsorption-desorption isotherms of MnO_2 and 0.25 mmol Cu^{2+} doped MnO_2 electrode

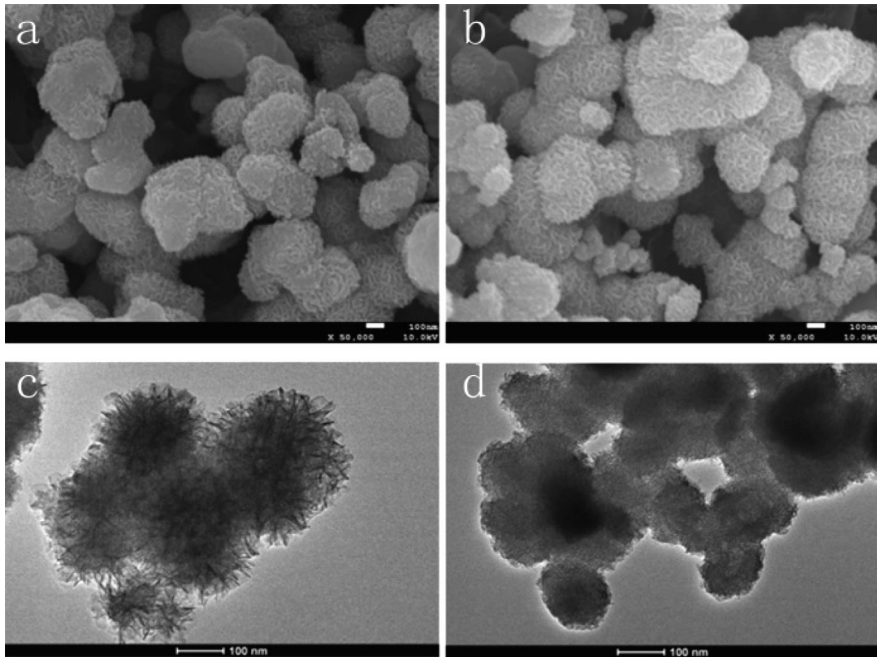

Fig. 2. SEM and TEM images of MnO_2 (a and c) and 0.25 mmol Cu^{2+}-doped MnO_2 (b and d)

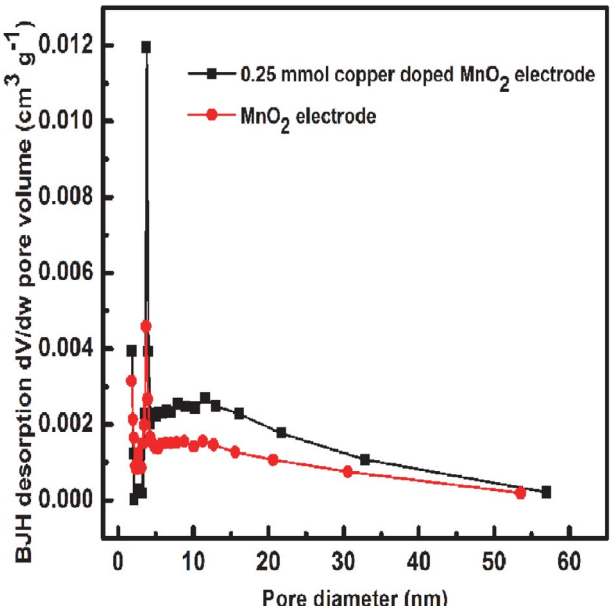

Fig. 4. BJH pore size distribution plot from the desorption branch of the MnO_2 and 0.25 mmol Cu^{2+} doped MnO_2 electrode.

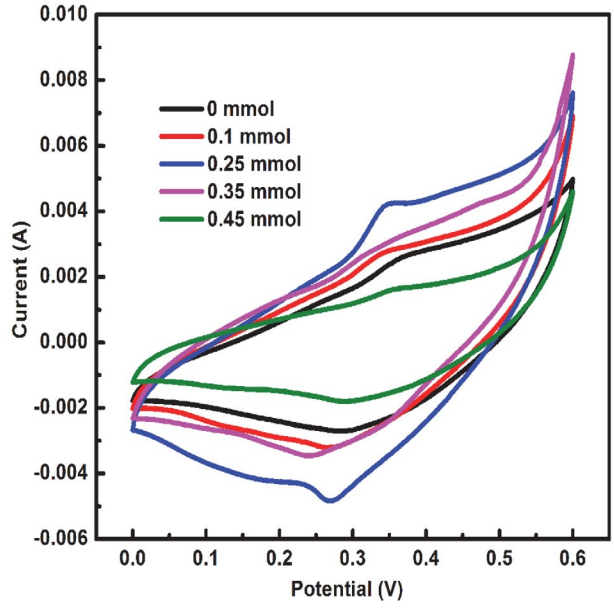

Fig. 5. CV curves of the as-prepared electrodes at 5 mV s^{-1}.

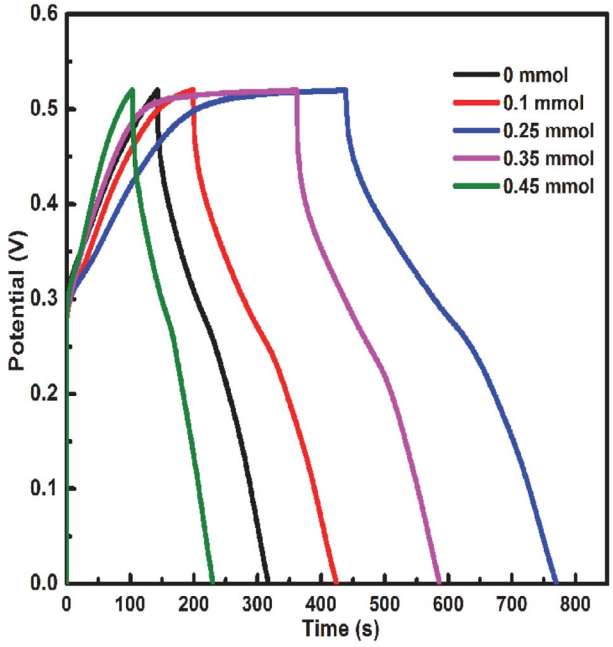

Fig. 6. Galvanostatic charge-discharge curves of as-prepared electrodes at a current density of 1 A g^{-1}.

≥ 0.45). The Brunauer-Emmett-Teller (BET) surface area of MnO_2 and 0.25 mmol Cu^{2+} doped MnO_2 is calculated to be 20.0 and 26.8 $m^2\ g^{-1}$, so the MnO_2 doped with Cu^{2+} can exhibit better electrochemical performance due to its larger surface area which can provide more electroactive sites for electrochemical reaction.[44] In addition, the Barrete-Joynere-Halenda (BJH) method was used to further determine the pore size distribution of the two samples by desorption isotherms (Figure. 4). The pore volumes of MnO_2 and 0.25 mmol Cu^{2+} doped MnO_2 are 0.067 and 0.10 $cm^3\ g^{-1}$, respectively. According to the pore size distribution of the corresponding desorption branches of the nitrogen adsorption isotherm, the average pore sizes of the two samples are 13.4 and 14.8 nm, indicating that they are mesoporous. Therefore, it is shown that the doping of copper ions has an effect on the surface area and pore size of MnO_2, thus improving the electrochemical performance.

3. 2. Electrochemical Performance

To investigate its electrochemical performance thoroughly, the electrochemical behavior of pure MnO_2 and Cu^{2+}-doped MnO_2 solid electrodes was studied by cyclic voltammograms (CV), galvanostatic charge-discharge (GCD), and electrochemical impedance spectroscopy (EIS). Figure 5 demonstrates the CV curves for MnO_2 and Cu^{2+}-doped MnO_2 with different proportions at the scan rate of 5 mV s^{-1} in the potential window of 0 to 0.6 V in 1 M KOH electrolyte. This figure shows that 0.25 mmol Cu^{2+}-doped MnO_2 exhibits the largest coverage area and the highest current, which indicates its ideal pseudo-capacitance properties and rapid charging and discharge processes. Figure. 6 shows the GCD cures of MnO_2 and Cu^{2+}-doped MnO_2 electrodes with current density ranging from 1 to 10 A g^{-1} in the 0-0.52 V voltage window. It shows that the electrode has the longest discharge time when the amount of doped copper is 0.25 mmol. The specific capacitance of the corresponding MnO_2 electrode calculated from this GCD curves is shown in Figure. 7. The results show that the specific capacitance of the electrodes by pure MnO_2 and Cu^{2+}-doped MnO_2 with different copper contents are 335.6, 433.5, 636.3, 431.9 and 243.7 F g^{-1} at current density of 1 A g^{-1}, respectively.

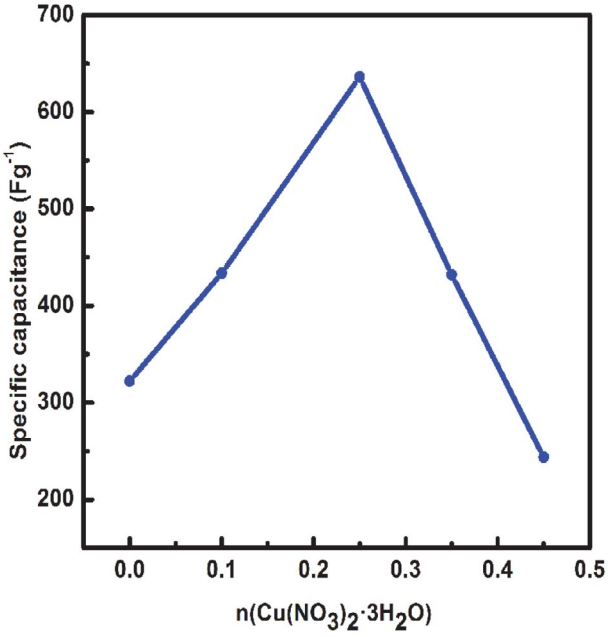

Fig. 7. Capacitance comparison curve of MnO_2 electrode doped with Cu^{2+} with different copper proportions.

Figure. 8 shows the CV curves of 0.25 mmol Cu^{2+}-doped MnO_2 at the scan rate of 5 mV s^{-1} at a potential window of 0 to 0.6 V. It can be seen that the MnO_2 with 0.25 mmol Cu^{2+} has regular and symmetrical shape, which proves that it has the typical pseudo-capacitance properties in the process of rapid charging and discharging. When the scanning rate is increased from 5 mV s^{-1} to 100 mV s^{-1}, the specific capacitance tends to decrease gradually. The CV curve is nearly symmetrical in the voltage window from 0 to 0.6 V without noticeable deflection, indicating its desirable reversibility and stability. This proportionality corresponds to the behavior of ideal capacitors.[45] Figure. 9 shows the GCD process of 0.25 mmol Cu^{2+}-doped MnO_2 electrodes. As the current density increases, the discharge time decreases, so the capacitance becomes smaller. Moreover, when the current density is 1A g^{-1}, the capacitance of 0.25 mmol Cu^{2+}-doped MnO_2 electrode is 636.3 F g^{-1}, which is nearly twice as high as that of pure MnO_2 (335.6 F g^{-1} at the current density of 1 A g^{-1}). The almost symmetrical charge / discharge curves further confirm the ideal charge-discharge characteristics and excellent reversibility, which is in good agreement with the CV curves. The charge-discharge curve deviates from the straight line obviously, especially the curves obtained at low currents, indicating the pseudo-capacitance behavior of the composite material. When the current density is low, the ions have enough time to penetrate and enter the interior. However, under the condition of high current density, due to the rapid charge / discharge time, the internal components cannot be used effectively, resulting in weaker electrochemical performance.[46] In order to further understand the transport kinetics of electrochemical behavior, the EIS spectra of MnO_2 and 0.25 mmol Cu^{2+}-doped MnO_2 electrode shown in Figure. 10 were obtained at open circuit potential in the frequency range from 0.01 Hz to 100 kHz. Typically, R_s (the composite resistance of electrolyte resistance, inherent resistance of substrate and contact resistance at active material / collector interface) can be obtained from the point where high frequency semicircle intersects crosses real resistance axis. And the Warburg impedances can be obtained from the slope of the diagram near the straight line in the low frequency region, and the larger the slope is, the smaller the resistance

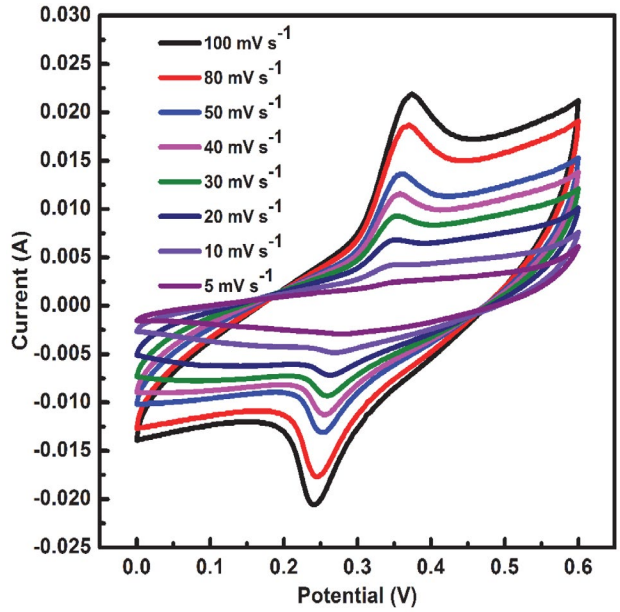

Fig. 8. CV curves of 0.25 mmol Cu^{2+}-doped MnO_2 electrode at various scan rates.

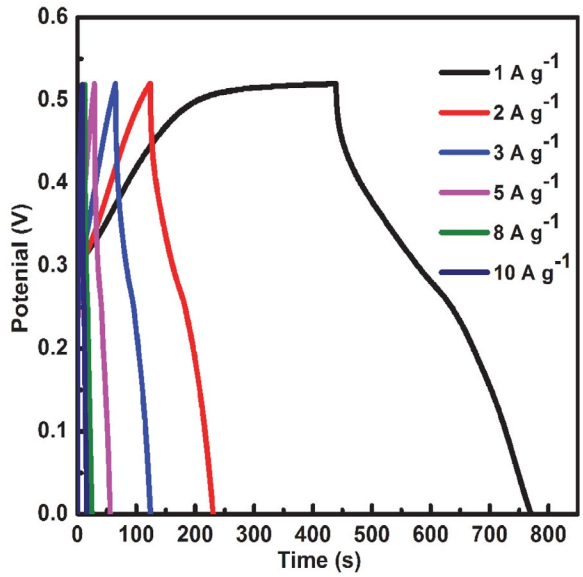

Fig. 9. Charge-discharge curves of the 0.25 mmol Cu^{2+}-doped MnO_2 electrode at different current density.

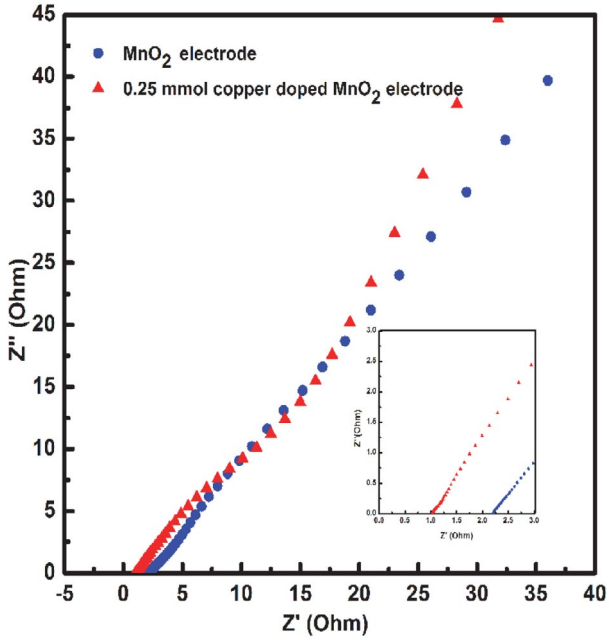

Fig. 10. Nyquist plots of the as-prepared electrodes.

is.[47,48] As shown in figure 10, the intersection point between Cu^{2+}-doped MnO_2 electrode and point axis is smaller than that of MnO_2, so the R_s of Cu^{2+}-doped MnO_2 is lower than that of MnO_2. In addition, the slope of Cu^{2+}-MnO_2 electrode is larger than that of MnO_2 electrode, so the Weinberg impedance is smaller. Since the electrolyte solution resistance of the two electrodes and the intrinsic resistance of NF should be the same, it can be concluded that the doping of Cu^{2+} reduces the R_s and Weinberg impedance of the MnO_2 electrode and decreases the contact resistance between the MnO_2 / NF interfaces.

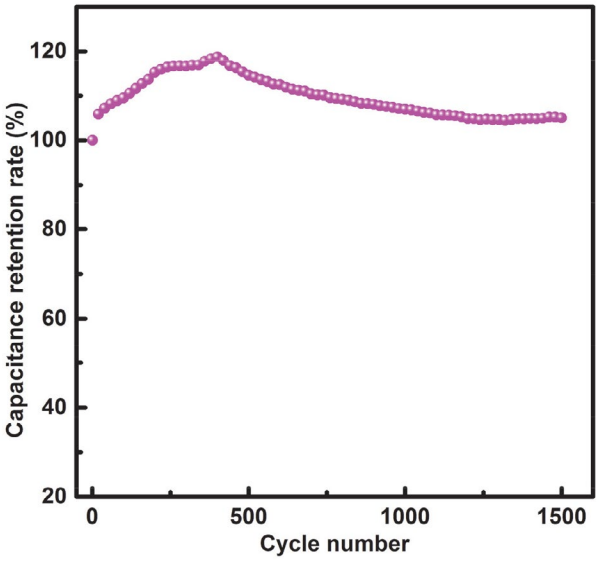

Fig. 11. Cycling stability of the 0.25 mmol Cu^{2+}-doped MnO_2 electrodes at 5 A g^{-1}.

In order to further demonstrate the superior performance of the as-synthesized 0.25 mmol copper doped MnO_2 electrode, as shown in Figure. 11, the long-term stability test of the 1500 cycles at the current density of 5A g^{-1} was carried out. From figure 11, it can be seen that the capacitance retention ratio of 1 to 500 cycles increases as the capacitance increases with the number of cycles. This is because the Cu^{2+}-doped MnO_2 is in an activated state during this process, and the activity gradually increases. After 500 cycles, the capacitance began to decrease slowly. Yet, even after 1500 cycles, the capacitance was still very good, showing a capacitance retention rate of 105.01% compared with the initial capacitance (100%) showing a good cycle stability.

4. Conclusions

In this work, Cu^{2+}-doped MnO_2 were synthesized by hydrothermal method and the optimum doping amount of Cu^{2+} was investigated. The results of XRD, SEM, TEM, BET test showed that the prepared samples' structure, morphology and pore distributions. The experimental results show that the 0.25 mmol Cu^{2+}-doped MnO_2 sample is expected to provide higher specific capacitance (636.3 F g^{-1} at 1 A g^{-1} current density) compared with pure δ-MnO_2 (335.6 F g^{-1} at the current density of 1 A g^{-1}) and long-term cyclic stability (105.01% capacitance retention after 1500 cycles at current density of 5 A g^{-1}). The EIS proved the lower resistance characteristics of the prepared electrodes. All the results show that the doping of Cu^{2+} has great influence on the improvement of MnO_2 electrochemical performance. The results are expected to pave the way for the development of low-cost and high-performance supercapacitors and other energy storage devices.

5. Acknowledgment

This work was supported by the National Natural Science Foundation of China [grant numbers 51302062].

6. References

1. M. Armand and J. M. Tarascon, *Nature* **2008**, *451*, 652–657. **DOI:**10.1038/451652a
2. M. M. Vadiyar, S. C. Bhise, S. S. Kolekar, J. Y. Chang, K. S. Ghule and A. V. Ghule, *Journal of Materials Chemistry A* **2016**, *4*, 3504–3512. **DOI:**10.1039/C5TA09022A
3. V. Augustyn, P. Simon and B. Dunn, *Energy & Environmental Science* **2014**, *7*, 1597–1614. **DOI:**10.1039/c3ee44164d
4. Q. Yang, Q. Li, Z. Yan, X. Hu, L. Kang, Z. Lei and Z. H. Liu, *Electrochimica Acta* **2014**, *129*, 237–244. **DOI:**10.1016/j.electacta.2014.02.113

5. G. A. Ferrero, M. Sevilla and A. B. Fuertes, *Sustainable Energy & Fuels* **2017**, *1*, 127. **DOI:**10.1039/C6SE00047A
6. P. Simon and Y. Gogotsi, *Nature Materials* **2008**, *7*, 845–854. **DOI:**10.1038/nmat2297
7. G. Wang, L. Zhang and J. Zhang, *Chemical Society Reviews* **2012**, *43*, 797–828. **DOI:**10.1039/C1CS15060J
8. R. Kötz and M. Carlen, *Electrochimica Acta* **2000**, *45*, 2483–2498. **DOI:**10.1016/S0013-4686(00)00354-6
9. C. Liu, F. Li, L. P. Ma and H. M. Cheng, *Advanced Materials* **2010,** *22***,** E28-E62. **DOI:**10.1002/adma.200903328
10. L. Yuan, X. H. Lu, X. Xiao, T. Zhai, J. Dai, F. Zhang, B. Hu, X. Wang, L. Gong and J. Chen, *Acs Nano* **2012**, *6*, 656. **DOI:**10.1021/nn2041279
11. C. Meng, C. Liu, L. Chen, C. Hu and S. Fan, *Nano Letters* **2010**, *10*, 4025–4031. **DOI:**10.1021/nl1019672
12. P. Yang, Y. Ding, Z. Lin, Z. Chen, Y. Li, P. Qiang, M. Ebrahimi, W. Mai, C. P. Wong and Z. L. Wang, *Nano Letters* **2014**, *14*, 731. **DOI:**10.1021/nl404008e
13. L. Peng, X. Peng, B. Liu, C. Wu, Y. Xie and G. Yu, *Nano Letters* **2013**, *13*, 2151–2157. **DOI:**10.1021/nl400600x
14. Y. Wang and Y. Xia, *Advanced Materials* **2013**, *25*, 5336–42. **DOI:**10.1002/adma.201301932
15. M. Zhi, C. Xiang, J. Li, M. Li and N. Wu, *Nanoscale* **2013**, *5*, 72–88. **DOI:**10.1039/C2NR32040A
16. C. C. Hu, K. H. Chang, M. C. Lin and Y. T. Wu, *Nano Letters* **2006**, *6*, 2690–2695. **DOI:**10.1021/nl061576a
17. D. Han, P. Xu, X. Jing, J. Wang, P. Yang, Q. Shen, J. Liu, D. Song, Z. Gao and M. Zhang, *Journal of Power Sources* **2013**, *235*, 45–53. **DOI:**10.1016/j.jpowsour.2013.01.180
18. Y. Xiao, C. Hu and M. Cao, *Journal of Power Sources* **2014**, *247*, 49–56. **DOI:**10.1016/j.jpowsour.2013.08.069
19. Y. Wei, C. W. Ryu and K. B. Kim, *Journal of Power Sources* **2007**, *165*, 386–392. **DOI:**10.1016/j.jpowsour.2006.12.016
20. M. M. Vadiyar, S. S. Kolekar, J. Y. Chang, A. A. Kashale and A. V. Ghule, *Electrochimica Acta* **2016**, *222,* 1604–1615. **DOI:**10.1016/j.electacta.2016.11.146
21. R. B. Rakhi, B. Ahmed, D. Anjum and H. N. Alshareef, *Acs Applied Materials & Interfaces* **2016**, *8*, 18806. **DOI:**10.1021/acsami.6b04481
22. Y. Han, S. Zhang, N. Shen, D. Li and X. Li, *Materials Letters* **2017**, *188*, 1–4. **DOI:**10.1016/j.matlet.2016.09.051
23. Q. X. Xia, J. M. Yun, R. S. Mane, L. Li, J. Fu, J. H. Lim and K. H. Kim, *Sustainable Energy & Fuels* **2017**, *1*, 529–539. **DOI:**10.1039/C6SE00085A
24. Z. Peng, X. Liu, H. Meng, Z. Li, B. Li, Z. Liu and S. Liu, *Acs Applied Materials & Interfaces* **2016**, *9,* 4577–4586. **DOI:**10.1021/acsami.6b12532
25. Y. Zhang, J. Zheng, Y. Zhao, T. Hu, Z. Gao and C. Meng, *Applied Surface Science* **2016**, *377*, 385–393. **DOI:**10.1016/j.apsusc.2016.03.180
26. W. Zhong, L. Lin, J. M. Yan and X. B. Zhang, *Advanced Science* **2017**, *4*, 1600382. **DOI:**10.1002/advs.201600382
27. J. Song, H. Li, S. Li, H. Zhu, Y. Ge, S. Wang, X. Feng and Y. Liu, *New Journal of Chemistry* **2017**, *41,* 3750–3757. **DOI:**10.1039/C6NJ04118C
28. W. Li, K. Xu, L. An, F. Jiang, X. Zhou, J. Yang, Z. Chen, R. Zou and J. Hu, *Journal of Materials Chemistry A* **2014**, *2*, 1443–1447. **DOI:**10.1039/C3TA14182A
29. Z. Song, W. Liu, M. Zhao, Y. Zhang, G. Liu, C. Yu and J. Qiu, *Journal of Alloys & Compounds* **2013**, *560*, 151–155. **DOI:**10.1016/j.jallcom.2013.01.117
30. W. HY, X. FX, Y. L, L. B and L. XW, *Small* **2014**, *10*, 3181–3186. **DOI:**10.1002/smll.201303836
31. W. Li, K. Xu, B. Li, J. Sun, F. Jiang, Z. Yu, R. Zou, Z. Chen and J. Hu, *Chemelectrochem* **2014**, *1*, 1003–1008. **DOI:**10.1002/celc.201400006
32. W. Wei, X. Cui, W. Chen and D. G. Ivey, *Chemical Society Reviews* **2011**, *40*, 1697–1721. **DOI:**10.1039/C0CS00127A
33. J. Chang, M. Jin, F. Yao, T. H. Kim, V. T. Le, H. Yue, F. Gunes, B. Li, A. Ghosh and S. Xie, *Advanced Functional Materials* **2013**, *23*, 5074–5083. **DOI:**10.1002/adfm201301851
34. M. Huang, R. Mi, H. Liu, F. Li, X. L. Zhao, W. Zhang, S. X. He and Y. X. Zhang, *Journal of Power Sources* **2014**, *269*, 760–767. **DOI:**10.1016/j.jpowsour.2014.07.031
35. H. Ye, Y. Cheng, T. Hobson and L. Jie, *Nano Letters* **2010**, *10*, 2727. **DOI:**10.1021/nl101723g
36. M. Huang, Y. Zhang, F. Li, Z. Wang, Alamusi, N. Hu, Z. Wen and Q. Liu, *Sci Rep* **2014**, *4*, 4518. **DOI:**10.1038/srep04518
37. W. Li, G. Li, J. Sun, R. Zou, K. Xu, Y. Sun, Z. Chen, J. Yang and J. Hu, *Nanoscale* **2013**, *5*, 2901–8. **DOI:**10.1039/c3nr34140b
38. M. Huang, Y. Zhang, F. Li, L. Zhang, Z. Wen and Q. Liu, *Journal of Power Sources* **2014**, *252*, 98–106. **DOI:**10.1016/j.jpowsour.2013.12.030
39. D. J. Davis, T. N. Lambert, J. A. Vigil, M. A. Rodriguez, M. T. Brumbach, E. N. Coker and S. J. Limmer, *Journal of Physical Chemistry C* **2014**, *118*, 17342–17350. **DOI:**10.1021/jp5039865
40. S. Falahatgar, F. Ghodsi, F. Tepehan, G. Tepehan, I. Turhan, *Applied Surface Science* **2014**, *289*, 289–299. **DOI:**10.1016/j.apsusc.2013.10.153
41. R. Bayon, G.S. Vicente, A. Morales, *Solar Energy Materials and Solar Cells* **2010**, *94*, 998–1004. **DOI:**10.1016/j.solmat.2010.02.006
42. R. Chen, J. Yu and W. Xiao, *Journal of Materials Chemistry A* **2013**, *1*, 11682–11690. **DOI:**10.1039/c3ta12589k
43. V. Subramanian, H. Zhu and B. Wei, *Journal of Power Sources* **2006**, *159*, 361–364. **DOI:**10.1016/j.jpowsour.2006.04.012
44. S. Lu, D. Yan, L. Chen, G. Zhu, H. Xu and A. Yu, *Materials Letters* **2016**, *168*, 40–43. **DOI:**10.1016/j.matlet.2016.01.021
45. Z. Cheng, G. Tan, Y. Qiu, B. Guo, F. Cheng and H. Fan, *Journal of Materials Chemistry C* **2015**, *3*, 6166–6171. **DOI:**10.1039/C5TC00645G
46. L. Ren, J. Chen, X. Wang, M. Zhi, J. Wu and X. Zhang, *Rsc Advances* **2015**, *5*, 30963–30969. **DOI:**10.1039/C5RA02663F
47. Y. C. Hsieh, K. T. Lee, Y. P. Lin, N. L. Wu and S. W. Donne, *Journal of Power Sources* **2008**, *177*, 660–664. **DOI:**10.1016/j.jpowsour.2007.11.026
48. C. W. Huang and H. Teng, *Salud Publica De Mexico* **2008**, *46*, 132–140.

Povzetek

S prilagajanjem množine dodanega $Cu(NO_3)_2 \cdot 3H_2O$ smo s preprostim hidrotermalnim sinteznim postopkom sintetizirali birnesite δ-MnO_2 dopiran z Cu^{2+}. Strukturo, morfologijo in specifično površino smo določili z naslednjimi metodami: rentgensko praškovno difrakcijo (XRD), vrstično elektronsko mikroskopijo (SEM), presevno elektronsko mikroskopijo (TEM) in meritvami specifične površine (BET). Nadaljnje študije so pokazale, da naj bi se pri vzorcu MnO_2, dopiranim z 0,25 mmol Cu^{2+}, zvišala specifična kapacitivnost (636,3 F g^{-1} pri gostoti toka 1 A g^{-1}) v primerjavi s čistim δ-MnO_2 (335,6 F g^{-1} pri gostoti toka 1 A g^{-1}) in dolgoročno ciklično stabilnost (105,01 % zadrževanje kapacitivnosti po 1500 ciklih pri gostoti toka 5 A g^{-1}). Z elektrokemijsko impedančno spektroskopijo (EIS) smo določili nizke upornosti pripravljenih vzorcev. Vsi rezultati kažejo, da je MnO_2 material, dopiran z bakrom mogoče pripraviti z razmeroma nizkimi stroški. Material pa ima tudi odlične elektrokemijski lastnosti in posledično velik potencial v prihodnjem razvoju energetike.